[35] M. A. Wieczorek, *Treatise on Geophyics*, T. Spohn, G. Schubert, eds. (Elsevier-Pergamon, Oxford, 2007), vol. 10, pp. 165–206.

[36] D. L. Turcotte, R. J. Willemann, W. F. Haxby, J. Norberry, *J. Geophys. Res.* **86**, 3951 (1981).

[37] D. E. Wilhelms, *The geologic history of the Moon*, vol. 1348 (U.S. Geol. Surv. Spec. Pap., 1987).

[38] H. J. Melosh, *Impact Cratering: A Geologic Process* (Oxford Univ. Press, New York, 1989).

[39] M. A. Wieczorek, F. J. Simons, *Geophys. J. Int.* **162**, 655 (2005).

[40] F. J. Simons, F. A. Dahlen, M. A. Wieczorek, *SIAM Rev.* **48**, 504 (2006).

[41] M. A. Wieczorek, F. J. Simons, *J. Fourier Anal. Appl.* **13**, 665 (2007).

[42] W. S. Kiefer, R. J. Macke, D. T. Britt, A. J. Irving, G. J. Consolmagno, *Second Conf. Lunar Highlands Crust* p. abstract 9006 (2012).

[43] R. Korotev, *Chemie der Erde, Geochemistry* **65**, 297 (2005).

[44] M. Ohtake, *et al.*, *Nature Geosci.* **5**, 384 (2012).

[45] R. J. Macke, D. T. Britt, G. J. Consolmagno, *Planet. Space Sci.* **58**, 421 (2010).

[46] J. Eluszkiewicz, *Icarus* **170**, 234 (2004).

[47] E. Rybacki, G. Dresen, *J. Geophys. Res.* **105**, 26017 (2000).

[48] S. Karato, P. Wu, *Science* **260**, 771 (1993).

[49] J. R. Driscoll, D. M. Healy, *Adv. Appl. Math.* **15**, 202 (1994).

[50] M. N. Toksöz, A. M. Dainty, S. C. Solomon, K. R. Anderson, *Rev. Geophys.* **12**, 539 (1974).

[51] M. T. Zuber, D. E. Smith, F. G. Lemoine, G. A. Neumann, *Science* **266**, 1839 (1994).

[52] G. A. Neumann, M. T. Zuber, D. E. Smith, F. G. Lemoine, *J. Geophys. Res.* **101**, 16,841 (1996).

[53] A. Khan, K. Mosegaard, K. K. L. Rasmussen, *Geophys. Res. Lett.* **27**, 1591 (2000).

[54] H. Chenet, P. Lognonné, M. Wieczorek, H. Mizutani, *Earth Planet. Sci. Lett.* **243**, 1 (2006).

[55] H. Hikida, M. A. Wieczorek, *Icarus* **192**, 150 (2007).

Supporting Online Material

www.sciencemag.org

SOM Text

Table S1

Figs. S1 to S12

References (35-55)

1 Density and porosity of the lunar crust from gravity and topography

The gravitational potential exterior to a planet can be expressed as [35]

$$U\left(\mathbf{r}\right) = \frac{GM}{r} \sum_{l=0}^{\infty} \sum_{m=-l}^{l} \left(\frac{R_0}{r}\right)^l C_{lm} \, Y_{lm}\left(\theta, \phi\right), \tag{1}$$

where $\mathbf{r}$ is position, G is the gravitational constant, M is the mass of the planet, R_0 is the reference radius of the spherical harmonic coefficients C_{lm} of degree l and order m, Y_{lm} are the 4π-normalized spherical harmonic functions, and θ and ϕ are colatitude and longitude, respectively. In this harmonic form, eq. (1) is exact for all radii greater than the maximum topographic excursion of the planet. If the relief h with respect to a spherical interface of radius D is expressed in spherical harmonics as

$$h\left(\theta, \phi\right) = \sum_{l=0}^{\infty} \sum_{m=-l}^{l} h_{lm} \, Y_{lm}\left(\theta, \phi\right), \tag{2}$$

the spherical harmonic coefficients of the gravitational potential resulting from a density contrast $\rho(\theta, \phi)$ can be calculated to arbitrary precision by the expression [26,35]

$$C_{lm} = \frac{4\pi \, D^3}{M(2l+1)} \sum_{n=1}^{N} \frac{(\rho \, h^n)_{lm}}{D^n \, n!} \frac{\prod_{j=1}^{n}(l+4-j)}{(l+3)}, \tag{3}$$

where the spherical harmonic coefficients of $\rho \, h^n$ are calculated according to

$$(\rho \, h^n)_{lm} = \frac{1}{4\pi} \int_{\Omega} \left[\rho(\theta, \phi) \, h^n(\theta, \phi)\right] Y_{lm}(\theta, \phi) \, d\Omega. \tag{4}$$

We use $N = 7$ when evaluating eq. (3), which gives a relative precision better than 10^{-4} at degree 400 for the surface relief of the Moon. The radial component of the gravity field is obtained by taking the radial derivative of eq. (1), and using the sign convection that gravity is positive when directed downwards, this is

$$g\left(\mathbf{r}\right) = \frac{GM}{r^2} \sum_{l=0}^{\infty} \sum_{m=-l}^{l} \left(\frac{R_0}{r}\right)^l (l+1) \, C_{lm} \, Y_{lm}\left(\theta, \phi\right). \tag{5}$$

The height of an equipotential surface above a reference radius R is, to first order,

$$N\left(\theta,\phi\right) \approx R \sum_{l=1}^{\infty} \sum_{m=-l}^{l} \left(\frac{R_0}{R}\right)^l C_{lm}\, Y_{lm}\left(\theta,\phi\right). \tag{6}$$

The degree-dependent relation between gravity g and topography h is quantified by the admittance

$$Z(l) = \frac{S_{hg}(l)}{S_{hh}(l)}, \tag{7}$$

and spectral correlation

$$\gamma(l) = \frac{S_{hg}(l)}{\sqrt{S_{hh}(l) S_{gg}(l)}}, \tag{8}$$

where the (cross)-power spectra S are

$$S_{hg}(l) = \sum_{m=-l}^{l} h_{lm}\, g_{lm}, \tag{9}$$

$$S_{hh}(l) = \sum_{m=-l}^{l} h_{lm}\, h_{lm}, \tag{10}$$

$$S_{gg}(l) = \sum_{m=-l}^{l} g_{lm}\, g_{lm}. \tag{11}$$

The observed gravity field of the Moon is a result of many factors, including surface topography, relief along the crust-mantle interface, core flattening, and heterogeneities in both the crust and mantle. Loads on the lithosphere, such as surface topography and volcanic intrusions, will cause the lithosphere to flex, giving rising to a signal from the crustal-mantle interface. Since gravitational signals are attenuated with increasing height above their depth of origin, and since the amount of flexure decreases with decreasing wavelength, the shortest wavelength anomalies will be sensitive primarily to relief along the surface. We quantify the influence of lithospheric flexure on the observed gravity field using a lithospheric loading model that incorporates surface loads on a thin elastic shell [36]. For this model, the admittance Z is simply the ratio of the gravity and topography coefficients in the spectral domain, and the spectral correlation γ is unity at all degrees.

For demonstration purposes, we use only the first order term in eq. (3), and calculate the admittance for several values of the elastic thickness T_e. As shown in Fig. S1, the admittance depends strongly on the elastic thickness at low degrees, but at high degrees, the admittance approaches an asymptotic value that is proportional to the crustal density. For elastic thicknesses greater than 5 km, the contribution to the gravity signal from lithospheric flexure is seen to be negligible at degrees greater than about 100. Even for an elastic thickness of zero, the admittance differs by less than 1% from that of a rigid shell at degrees greater than 170. Since it is unlikely that the elastic thickness would be zero for the shortest wavelengths, which are dominated by young impact craters, we neglect the flexural signal by analyzing degrees greater than 150.

Even though the GRAIL gravity field has been developed up to degree and order 420, the highest degree terms are biased by noise and incomplete sampling between adjacent orbital tracks. In Fig. S2, we plot the power spectrum of the gravity field, the measurement noise, the gravitational contribution from the surface topography (the Bouguer correction), and the gravitational signal that remains after removing the topographic contribution (the Bouguer anomaly). Beyond degree 320, the power spectrum of the Bouguer anomaly increases in amplitude and follows the gravitational error. In order to minimize the consequences of noise from the gravity field in our analysis, we make use of degrees less than 310.

If the density of the crust ρ_c were constant, the observed gravity g at short wavelengths would be equal to the sum of the Bouguer correction g^{BC} and the measurement noise g^{noise}. If the correct crustal density were chosen when calculating the Bouguer correction, the Bouguer anomaly g^{BA} would simply be equal to the noise in the gravity model

$$g_{lm}^{\mathrm{BA}}(\rho_c) = g_{lm} - g_{lm}^{\mathrm{BC}}(\rho_c) = g_{lm}^{\mathrm{noise}}. \tag{12}$$

Since the gravitational measurement noise should be uncorrelated with the surface topography, an unbiassed estimate of the crustal density is obtained by finding the value that minimizes the correlation between the Bouguer anomaly and topography.

We calculate the correlation coefficient of the gravity and topography in the space domain using gridded Bouguer gravity and topography within a spherical cap of a specified diameter. The gravity and topography coefficients are truncated below degree 150 and above degree 310, the gravity is downward continued to the average radius of the analysis region, and the gridded data are weighted by their associated areas. To neglect the gravitational contribution from the mare basalts, which are more dense than the highlands and which pool at low elevations, we neglect data points that lie with the mare using the map of ref. [37]. To assure that each analysis is based on similar effective areas, we neglect those analyses where more than 5% of the data have been discarded. Analyses were centered on a 60-km (2° of latitude) equally spaced grid, and the crustal density was varied to find the value that minimizes the absolute value of the correlation coefficient.

Estimates of the uncertainties in our density determinations were obtained by Monte Carlo modeling. Using of the known uncertainties of the global gravity field coefficients, noise in the Bouguer gravity field was simulated, and the probability distribution for the correlation coefficient between this noise and the topography was obtained. 1-σ error limits on the density were determined using the 68% confidence limits from the correlation coefficient probability distribution. To neglect regions with large uncertainties, a small number of analyses were discarded where the minimum correlation coefficient was greater than the 95% confidence limit.

Having calculated the bulk density from gravity and topography, we estimate the crustal porosity using independent estimates of the crustal grain density. An empirical correlation between grain density (estimated from a mineralogical norm) and the abundance of FeO and TiO_2 was obtained by ref. [12] for a large range of lunar rock compositions, including the ferroan anorthosites, Mg suite, alkali suite, KREEP basalts, impact melts, granulitic breccias, mare basalts and volcanic glasses. The mineralogical grain density estimates have been shown to be accurate to 20 kg m^{-3} by direct measurements using helium pycnometry techniques [14], and the correlation with iron and titanium abundances has an intrinsic uncertainty of 45 kg m^{-3} for the entire suite of lunar rocks. Using Lunar Prospector gamma-ray spectrometer derived iron and titanium abundances [13], which are representative of the upper meter of the surface, our global crustal grain density estimate is shown in Fig. S3. For each region in our gravity analyses, the average grain density was calculated, from which the porosity ϕ was determined from the relation

$$\phi = 1 - \rho_{\text{bulk}}/\rho_{\text{grain}}, \tag{13}$$

where the bulk density is the density obtained from the gravity analysis. Since impact caters excavate materials to depths that are about one-tenth of the crater diameter [38], the composition of the lunar surface is likely to be representative of the underlying crust for most regions of the Moon. Nevertheless, where the crustal composition changes laterally, such as between the highlands and South Pole-Aitken basin, or between the highlands and mare basalts, ejecta from one compositional unit may overlie surface materials of a different composition.

Histograms of our results using 360-km diameter analysis regions are shown in Fig. S4 for the bulk density, bulk density uncertainty, and porosity. Our bulk density and porosity determinations are insensitive to variations in the filter applied to the gravity and topography by more than ±50 degrees, as well as to changes in the size of the analysis region by a factor of two. Nevertheless, as the analysis region decreases in size, the uncertainties in the individual density determinations increase in magnitude. Porosity maps derived using several different sizes for the analysis regions are shown in Fig. S5.

We verify the accuracy of our bulk density determinations using an alternative analysis method that makes use of the relation between gravity and topography in the spectral domain. Since the gravity contribution from topography at high degrees is a non-linear function of the topography, we model the observed gravity in terms of the gravity contribution from surface relief of unit density, $\hat{g}$,

$$g_{lm}^{obs} = \rho_c \, \hat{g}_{lm} + I_{lm}, \tag{14}$$

where I_{lm} is that portion of the signal not predicted by the model, and which is assumed to be uncorrelated with $\hat{g}$. Multiplying both sides by $\hat{g}_{lm}$, summing over all degrees, and taking the expectation with respect to I, we obtain an unbiased estimate for the crustal density at each degree,

$$\rho_c(l) = \frac{S_{g^{\rm obs}\hat{g}}(l)}{S_{\hat{g}\hat{g}}(l)}. \tag{15}$$

This equation is analogous to the admittance between gravity and topography from eq. (7).

We spatially localize the free-air gravity and gravity from unit density topography using the spherical Slepian functions of refs [39–41] and then compute the localized degree-dependent admittance and correlation functions, eqs (14) and (8). The spectral bandwidth L of the window was chosen to ensure that more than 99% of its power was localized within a spherical cap of a specified diameter. Since each degree l of the localized power spectrum has contributions from the global field from degrees $l - L$ to $l + L$, we calculate the average density for all degrees between $150 + L$ and $310 - L$. As the localized correlation should be nearly unity for uncompensated topography, those degrees with localized correlations less than 0.98 where discarded. If more than half of the degrees available for analysis were discarded, or if the analysis region contained more than 5% mare basalts, the analysis was discarded as well.

Our bulk density estimates using this spectral approach are shown in Fig. S6 using a localization window with a diameter of 540 km and a spectral bandwidth of $L = 28$. The average density of the highlands is found to be identical to that obtained from our space domain analysis. Minor differences in the lateral variations exist between Figs 1 and S6 that are a result of slightly different aspects of the two analysis techniques: The spectral approach is not capable of removing small regions of mare basalts in an analysis region, the spatio-spectral localization

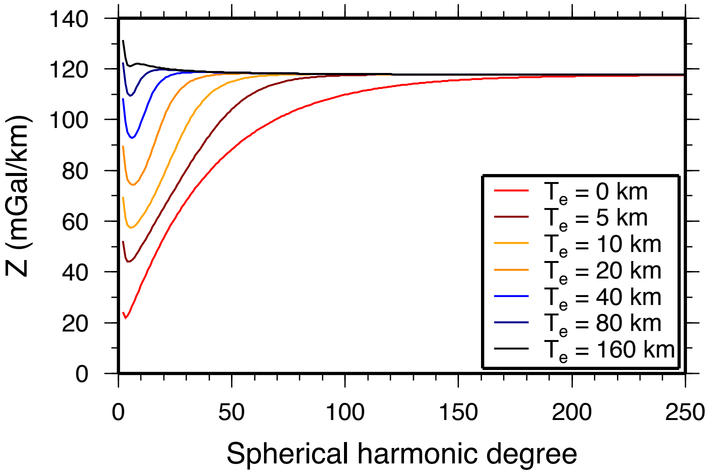

Fig. S1. Gravitational admittance as a function of spherical harmonic degree for a lithospheric loading model that includes surface loads on a thin elastic spherical shell. The admittance is sensitive to the assumed elastic thickness at low degrees, but approaches an asymptotic value that is proportional to the crustal density at high degrees.

window is not uniform in amplitude like the ‘box car’ window used in the space domain analysis, and since the gravity signal is largest at the lowest degrees, the space domain analysis is somewhat more sensitive to the lowest degrees (Fig. S2), whereas the spectral approach weights each degree evenly.

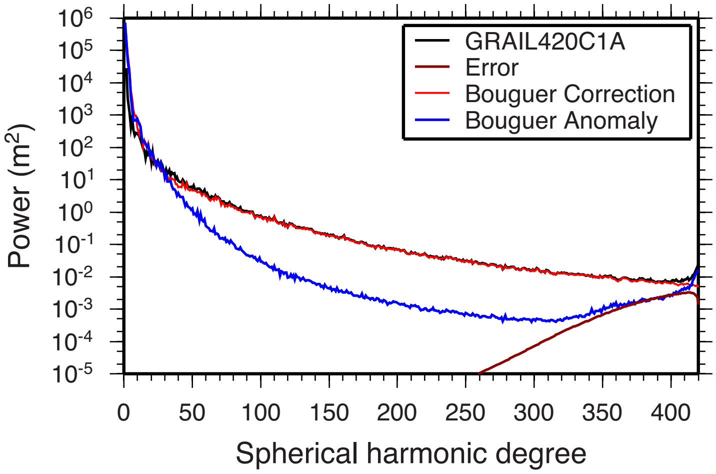

Fig. S2. Geoid power spectra of the GRAIL gravity model, the model errors, the Bouguer correction, and the Bouguer anomaly. Beyond degree 320, the Bouguer anomaly increases in amplitude and follows the model error spectrum.

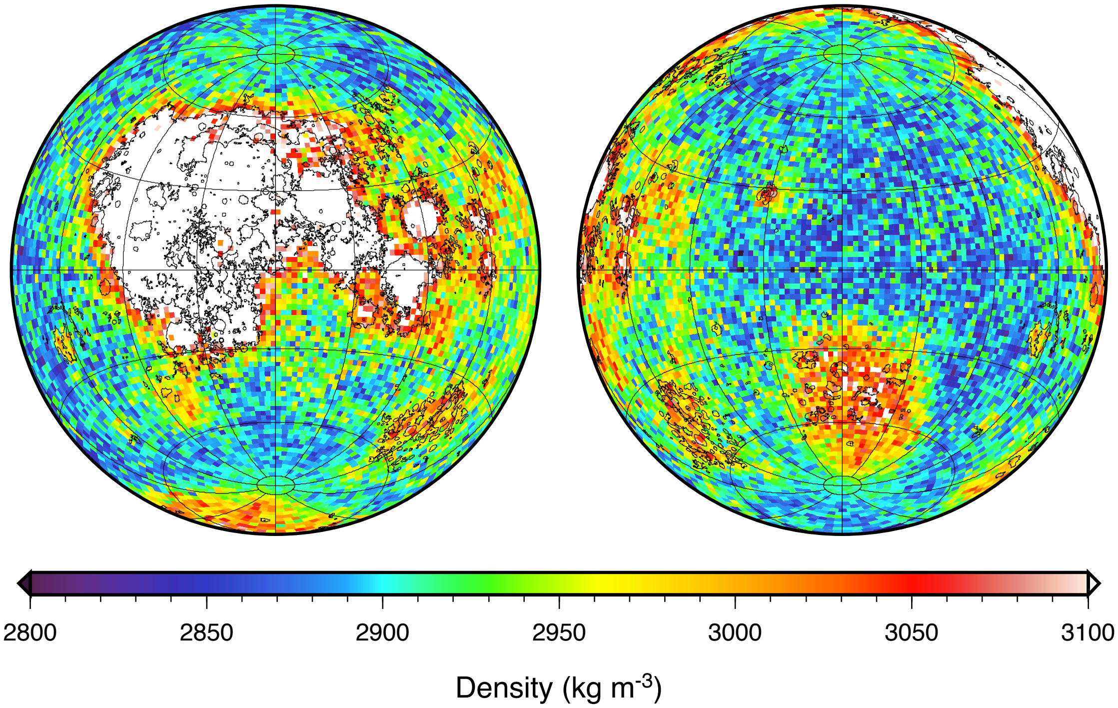

Fig. S3. Crustal grain density estimated from the 2° Lunar Prospector iron and titanium abundances and a sample-based empirical correlation between grain density and composition. Thin lines outline the locations of the mare basalts. Data are presented in two Lambert azimuthal equal-area projections centered over the near (left) and far (right) side hemispheres, with each image covering 75% of the lunar surface, and with gridlines being spaced every 30°.

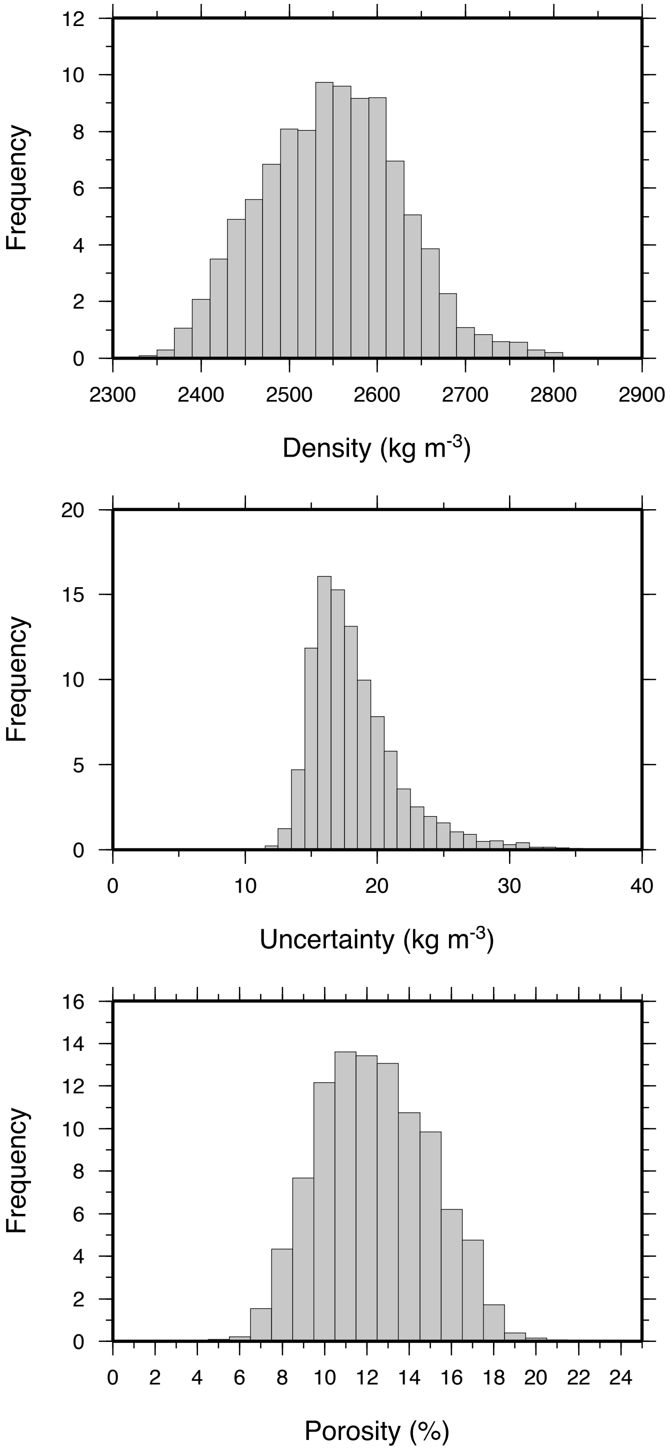

Fig. S4. Histograms of bulk density, bulk density uncertainty, and porosity for the lunar highlands using Bouguer gravity and topography within 360-km diameter circles.

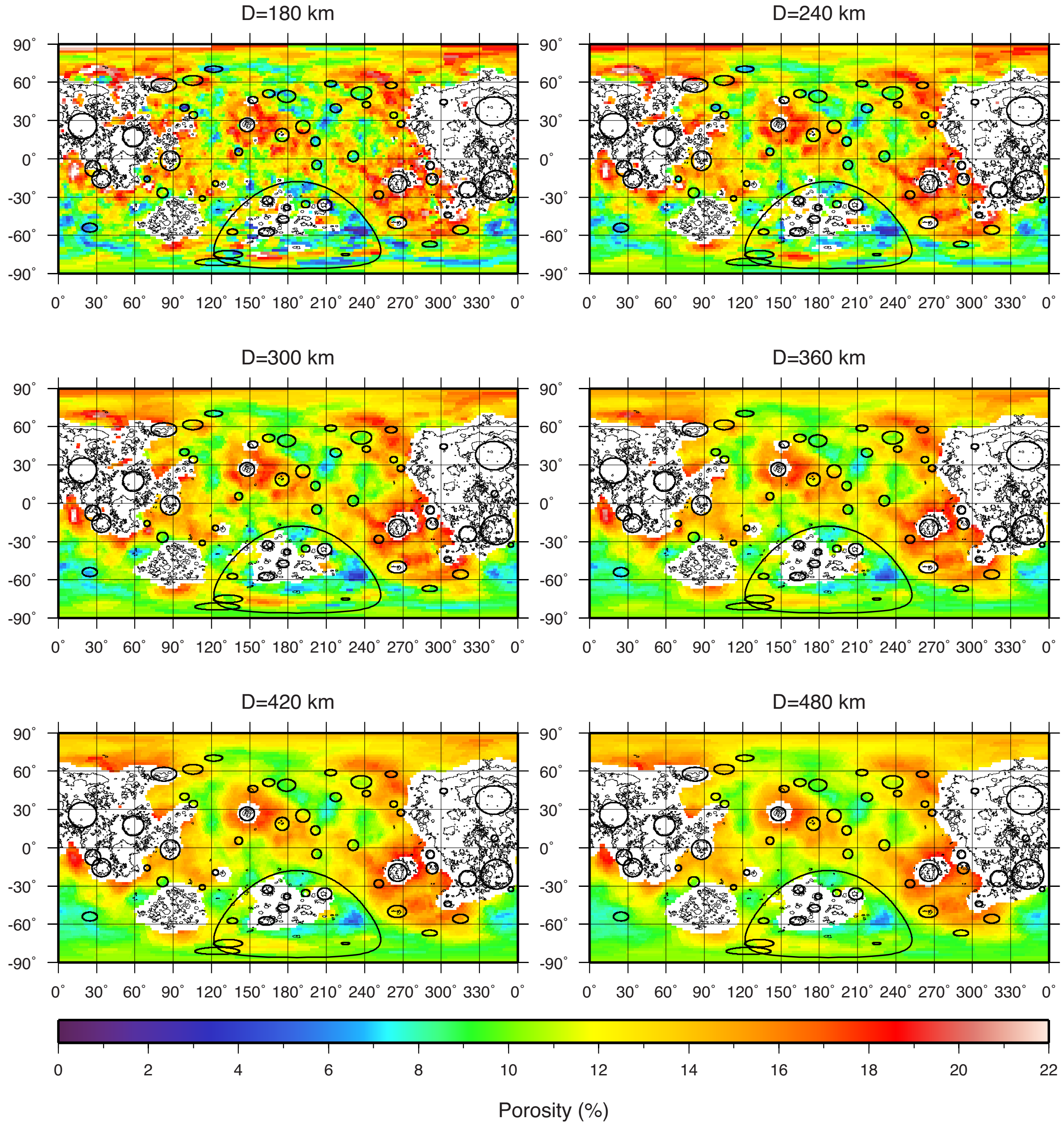

Fig. S5. Porosity of the lunar crust from gravity, topography, and independent grain density estimates. Thin lines outline the mare basalts, and circles denote the region of crustal thinning for prominent impact basins from Fig. 3. Bulk densities and porosities were calculated using data within circles with diameters of 180, 240, 300, 360, 420, 480 km, which corresponds to 6, 8, 10, 12, 14, and 16 degrees of latitude, respectively. All images are shown in a cylindrical projection centered over the far side hemisphere.

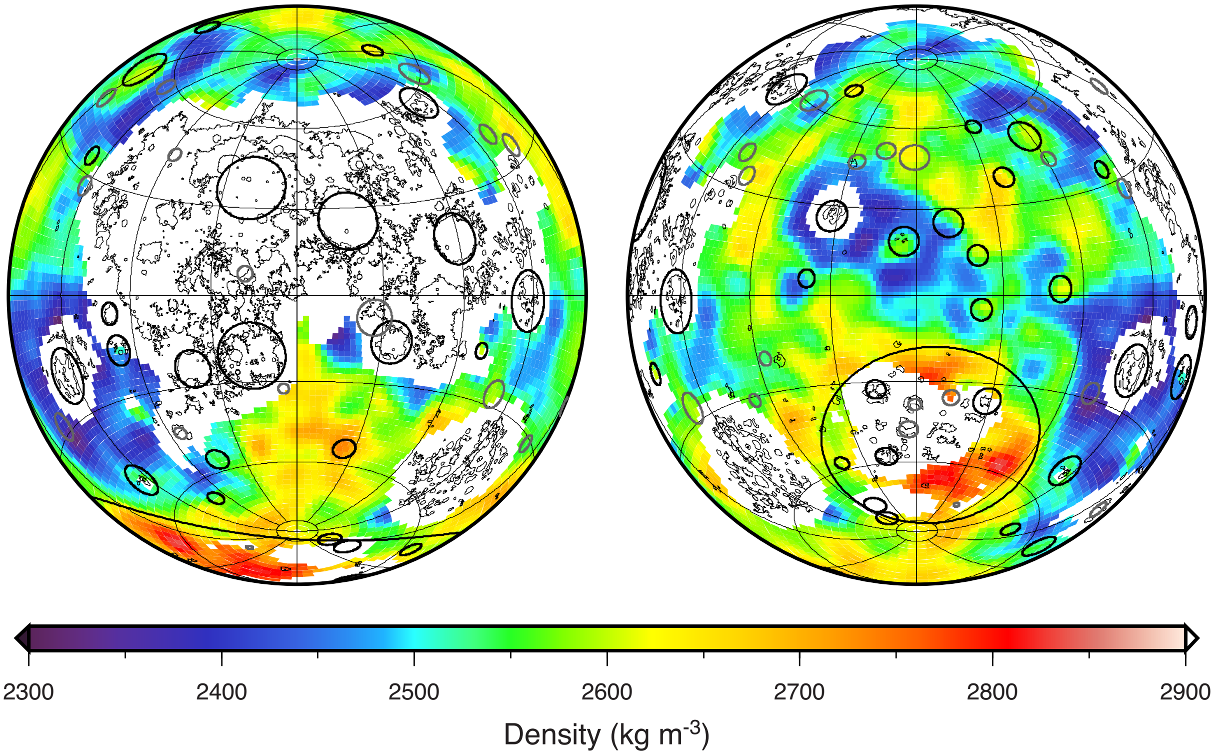

Fig. S6. Bulk density of the lunar crust from a localized spectral analysis approach. At each point on a 60-km equally spaced grid, the free-air gravity and predicted gravity from topography with unit density were multiplied by a localization window with a diameter of 540 km (18° of latitude). The bulk density was determined as the average of eq. (15). Image format the same as Fig. S3.

2 Depth dependence of porosity

If the density of the lunar crust were constant with depth, eq. (3) could be used to calculate the gravity above the surface. This is was the basis of our bulk crustal density determinations described in Section 1. If the crustal density were instead a function of depth below the surface, the lateral variations in density along a spherical interface below the surface would give rise to an additional gravitational signal. These gravity signals would be attenuated both with increasing depth and with increasing spherical harmonic degree (see eq. (1)). We use the wavelength dependence of this subsurface signal to investigate the subsurface density profile. Two models were investigated: one where the porosity decreased exponentially with depth below the surface, and another where a constant thickness porous layer overlies a non-porous basement. By discretizing the density profile in depth, the expected gravitational signature can be calculated to arbitrary precision from eq. (3) for each layer. We calculate the synthetic admittance for each density profile, and then compare this to observations.

Synthetic admittance functions are shown in Fig. S7 for several assumed porosity structures of the crust, all which assume a grain density of 2900 kg m^{-3}. Two end-member models with zero and 12% porosity are seen to be related by a simple multiplicative constant involving the ratio of the two bulk densities. The other models have density profiles and admittances bracketed by these end members. For one set of models, we assume that a 5 or 30 km thick layer with 12% porosity overlies non-porous bedrock. At small degrees, the admittance approaches the value predicted for the zero porosity model, whereas at the largest degrees, the admittance approaches the value predicted for the constant 12% porosity model. This is easily understood as the shortest wavelength signals become increasingly attenuated with increasing depth below the surface. At the shortest wavelengths, the gravity field is simply a result of the density of the surface relief. Models that utilize an exponential decrease in porosity with depth yield very similar results if the depth of the porous layer D is replaced by the e-folding depth λ, and if the porosity of the layer ϕ is replaced by the porosity at the surface ϕ_0.

For illustrative purposes, we calculate the global effective density from eq. (15) for a layer of thickness D and porosity ϕ under the assumption that the grain density is 2915 kg m^{-3}. This function gives the effective bulk density at each degree that would be obtained if it were assumed that the density of the crust was uniform. The rms misfit between this effective density and that obtained using the observed gravity field is shown in Fig. S8 using degrees between 150 and 310. A clear tradeoff is found between these two parameters, but a best fit is found for a layer thickness of 28 km and a porosity of 13%. Given that the gravity signal for the shortest wavelengths is attenuated with increasing depth, the admittance is largely insensitive to layer thickness in excess of about 30 km. Similar results are found for a model where the porosity decreases exponentially with depth.

We next use a spatio-spectral localization technique to calculate localized admittances, and then use Monte Carlo methods to estimate the 1-σ upper and lower bounds for the layer thickness and porosity. The procedure used is similar to that described in Section 1, except that here we use a localization window with a diameter of 900 km (corresponding to 30° of lattitude). By employing a larger window size, the spectral bandwidth of the window is reduced to $L = 17$, and this gives us a higher spectral resolution and a greater number of localized admittances to analyze. In Fig. S9, we plot the best-fit layer thickness and porosity, as well as the 1-σ upper and lower bounds. The porosity is found to be rather well constrained and is consistent with our analyses in Section 1. In contrast, the layer depth is not well constrained. For most of the highlands, the 1-σ upper bound is simply greater than about 40 km. Nevertheless, the 1-σ lower bound possess values from about zero to 31 km, implying that some regions of the Moon possess a porous layer that is 10s of km thick.

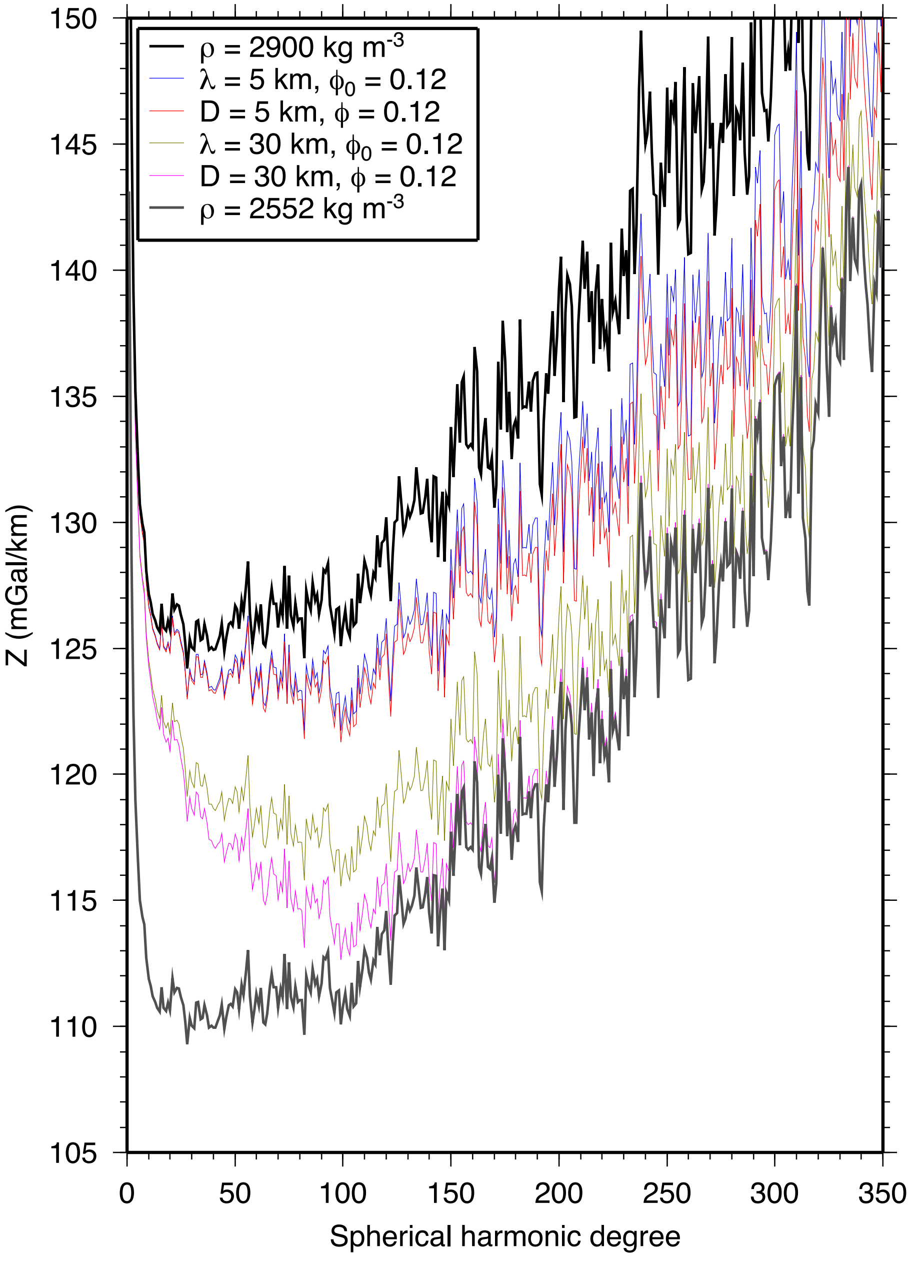

Fig. S7. Synthetic admittances predicted by several assumed density profiles of the highlands crust. Black and gray curves represent end-member cases with a constant bulk density of 2900 and 2552 kg m^{-3}, respectively. Red and magenta curves are for models where a layer of thickness D and porosity ϕ overlie non-porous bedrock. Blue and green curves are for models where the porosity decreases exponentially with depth with e-folding depth λ and surface porosity ϕ_0.

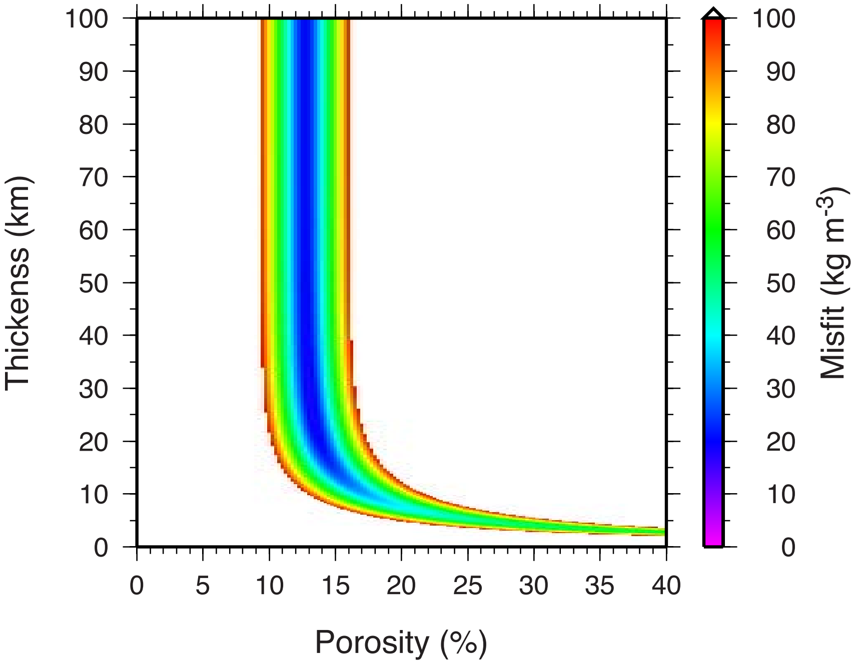

Fig. S8. RMS misfit for a model with a layer of constant thickness and porosity overlying non-porous bedrock. The misfit is the rms difference of the effective density $\rho_c(l)$ calculated from eq. (15) using both the model and observed gravity between degrees 150 and 310.

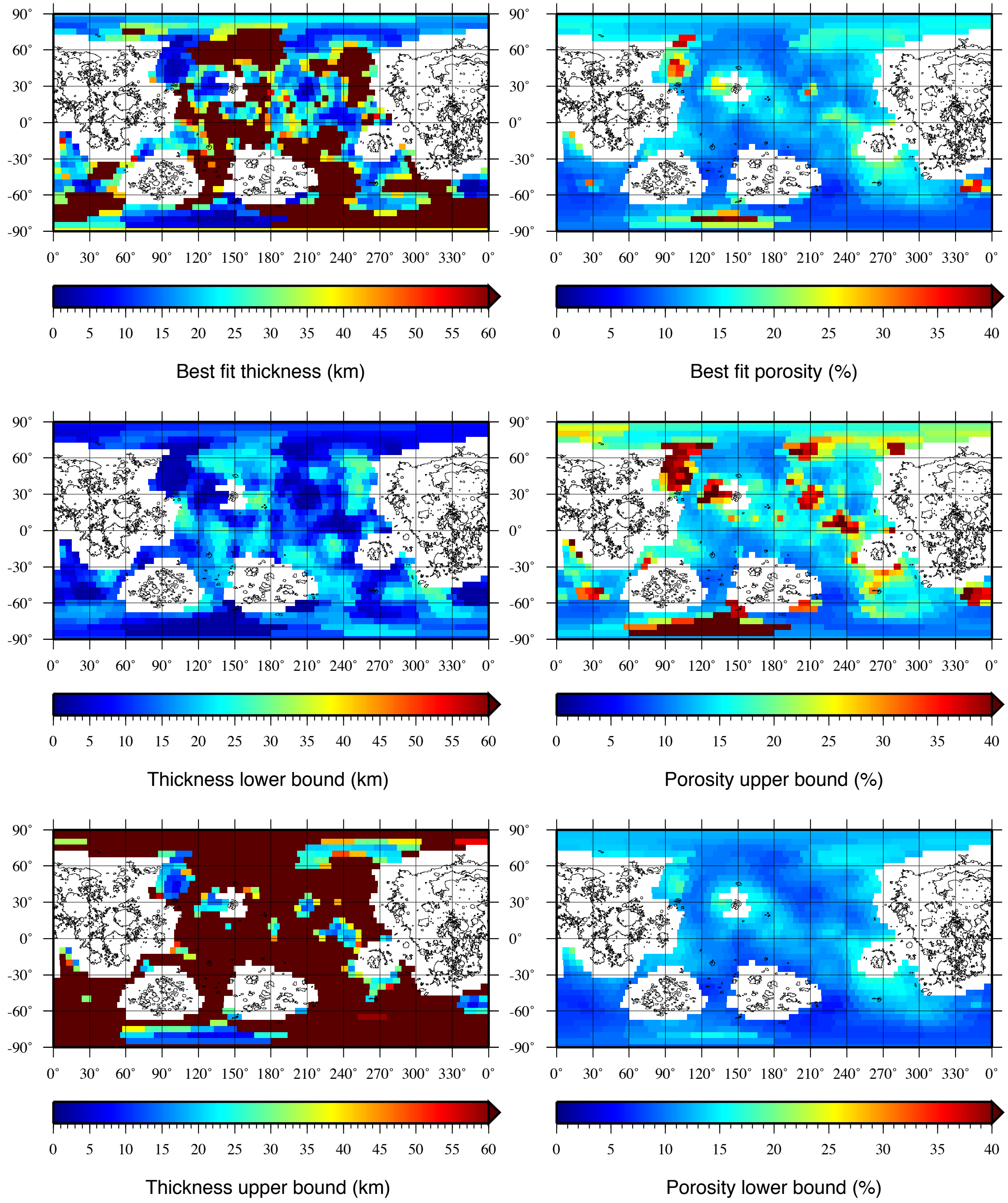

Fig. S9. Best fit layer thickness and porosity, as well as the 1-σ upper and lower bounds as determined from Monte Carlo modeling. For this analysis, localized inversions were performed using a window with 900 km diameter (corresponding to 30° of latitude).

3 Density and porosity of lunar samples

Measurements of the density and porosity of lunar feldspathic rocks, including samples collected during the Apollo program and lunar meteorites, provide a context for interpreting the results derived in this study. Twenty four feldspathic samples have been analyzed using modern techniques that contain 22-35 wt.% Al_2O_3, corresponding to 60-95% anorthite [14, 42]. The samples include a moderate abundance of mafic minerals, characterized by FeO+MgO of 0.5-18.9 wt.% and a range of magnesium numbers (the molar ratio Mg/(Mg+Fe)) from 0.44 to 0.80. By the inclusion of lunar meteorites in the data set, it is likely to be more representative of the Moon's global crust than would be the case for measurements of Apollo samples alone [43]. The FeO abundances and Mg numbers for these samples are similar to the ranges inferred for the lunar highlands in remote sensing data [13,44]. By igneous nomenclature, these rocks are anorthosites, noritic anorthosites, and anorthositic norites, although all of these rocks have experienced considerable post-igneous processing, such as brecciation, shock melting, and sometimes thermal annealing. The measured suite of feldspathic rocks is assumed to be representative of the range of impact processing experienced by rocks in the upper few kilometers of the lunar crust.

The bulk density of the rocks is based on the total volume that includes the effects of void space from porosity. This is the density that is appropriate for use in gravity modeling. Bulk density was measured by immersion of the sample in glass beads [15], and the grain density is based on the volume of solid material in the rock, excluding the effects of porosity, as measured using helium pycnometry methods [45]. The small atomic radius of helium allows it to diffuse through even very small cracks, and it has been shown that there is no unmeasured closed pore space in these samples [14]. From the bulk and grain densities, one can calculate the porosity from eq. (13). Measurement uncertainties are typically 30-70 kg m^{-3} for the bulk density and

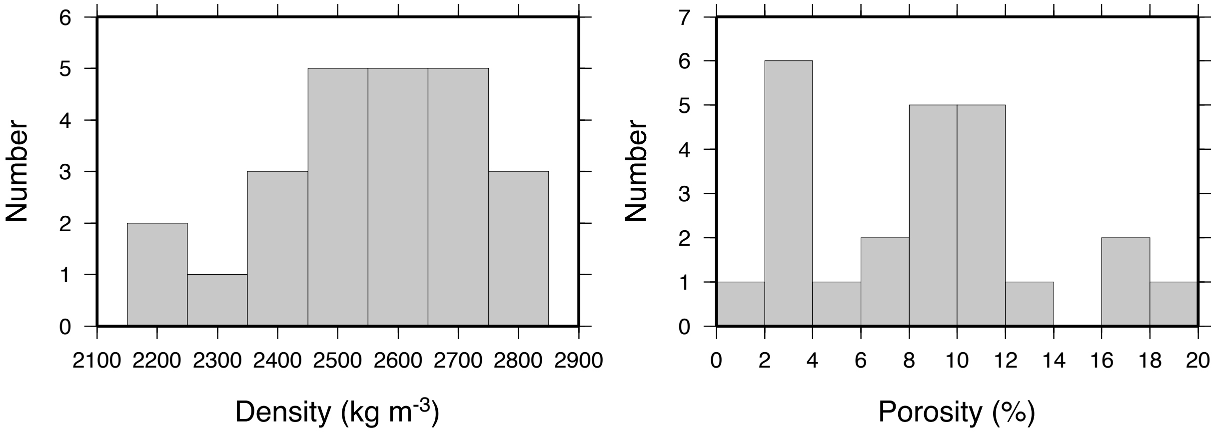

Fig. S10. Bulk density (left) and porosity (right) of twenty four feldspathiclunar rocks.

1-3% for porosity. Fig. S10 shows that the measured bulk densities have a broad, flat-topped histogram, with a mean density of 2580±170 kg m^{-3}, and that the porosities also have a broad distribution, with a mean of 8.6±5.3%.

4 Viscous closure of pore space

Rocks at elevated temperatures will flow if subjected to stress and this process can result in thermal annealing of porosity over long timescales. To calculate the time evolution of lunar porosity we follow the approach outlined in Appendix B of ref. [21]. Here, the porosity ϕ evolves according to

$$\frac{d\phi}{dt} = \phi \frac{\rho g z}{\eta} \tag{16}$$

where ρ is the crustal density, g is the acceleration due to gravity, z is depth below the surface and η is the viscosity. In general, viscosity is a function of both temperature and stress, and here we calculate η according to

$$\eta = \frac{P^{1-n}}{A} \exp\left(\frac{Q}{RT}\right) \tag{17}$$

where A and n are rheological parameters, Q is the activation energy, R is the gas constant, T is temperature, and the overburden pressure P is $\rho\, g\, z$. This approach is almost identical to that employed by ref. [46], and because of the strong temperature-dependence of viscosity, differences in the porous layer depth calculated by the two approaches are only about 1 km.

Given a temperature profile, equations (16) and (17) can be solved numerically to determine the porosity evolution as a function of time. Fig. S11 shows sets of normalized porosity profiles after 4 billions years of evolution for two different rheologies and different representative surface heat fluxes. As expected, initial near-surface porosity is unchanged because the viscosities are too high for flow to occur, while porosity at greater depth is reduced to zero. The transition interval is narrow because of the strong temperature-dependence of viscosity, and higher heat fluxes result in a thinner porous layer, as expected. Olivine (mantle) is less deformable than plagioclase (crust), and as a result, the olivine rheology has a porous layer that extends to depths that are about 15 km deeper than for crustal materials. This approach assumes implicitly that porosity is initially present and is not subsequently regenerated; such an assumption is at least

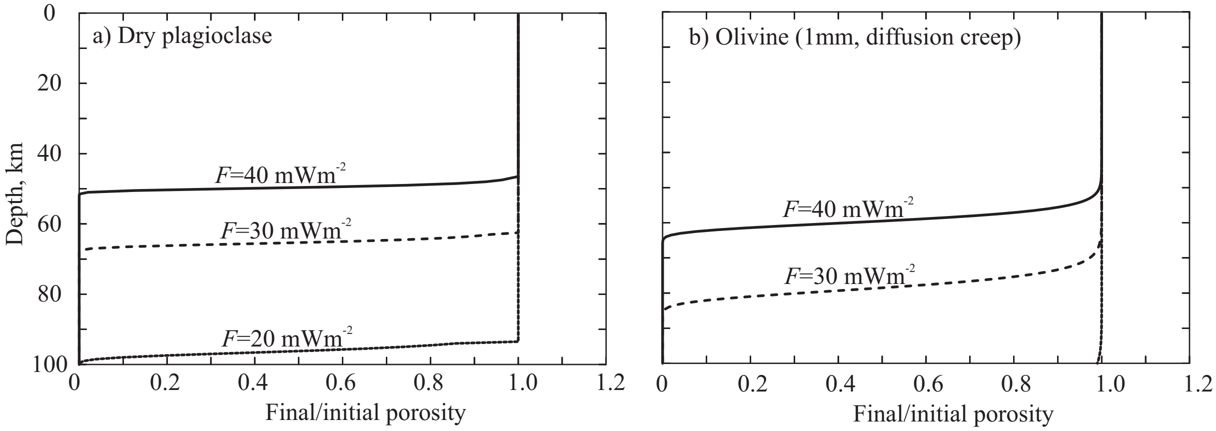

Fig. S11. Normalized porosity profiles after 4 billion years of evolution for (a) a dry plagioclase rheology and (b) a dry olivine rheology. The temperature structure is assumed constant with time and is calculated using surface heat fluxes F of $20, 30$ and 40 $\mathrm{mW\ m^{-2}}$. To produce these plots, we assumed a constant thermal conductivity of 3 W $\mathrm{m^{-1}\ K^{-1}}$, a surface temperature of 250 K, ρ=2800 kg $\mathrm{m^{-3}}$, and g=1.6 m $\mathrm{s^{-2}}$. The rheological parameters for dry plagioclase and olivine were taken from refs [47] and [48], respectively.

roughly consistent with the steeply declining impactor flux associated with the Moon.

5 Thickness of the lunar crust

We construct a global model for the thickness of the lunar crust that satisfies the observed gravity field and seismic constraints. For this model, the observed gravity is assumed to be a result of relief along the surface, relief along the crust-mantle interface (the 'Moho'), and lateral variations in density of the crust:

$$C_{lm}^{\rm obs} = C_{lm}^{\rm topo} + C_{lm}^{\rm Moho} + C_{lm}^{\rho}. \tag{18}$$

If the density of the crust depends upon position, but not depth, the first two terms can be calculated using eq. (3). For the first contribution, the surface relief is referenced to the mean planetary radius R of the Moon and possesses a density contrast $\rho(\theta, \phi)$, whereas for the second contribution, the relief of the crust-mantle interface is referenced to its mean radius D and possesses a density contrast $\rho_m - \rho(\theta, \phi)$. The gravitational contribution from lateral variations in density of the shell between the two radii R and D is calculated from the potential coefficients (referenced to radius R)

$$C_{lm}^{\rho} = \frac{4\pi R^3}{M(2l+1)(l+3)} \left(1 - (D/R)^{l+3}\right) \rho_{lm}, \tag{19}$$

where ρ_{lm} are the spherical harmonic coefficients of $\rho(\theta, \phi)$. In our model, we do not attempt to fit the total mass of the Moon (i.e., the term C_{00}), as this depends on the unknown density profile of the mantle and the size and composition of the core.

Given $C^{\rm obs}$, $C^{\rm topo}$, and C^{ρ}, and following ref. [26], we solve eq. (18) for the spherical harmonic coefficients of the first-order term of the Moho relief multiplied by the density contrast. The resulting non-linear equation is then solved in an iterative manner. First, given the ith estimate of the Moho relief, the spherical harmonic coefficients of the next estimate multiplied by the density contrast are calculated using

$$\left({}^{(i+1)}h\,\rho\right)_{lm} = \tag{20}$$

$$w_l \left[\frac{\left(C_{lm}^{\mathrm{obs}} - C_{lm}^{\mathrm{topo}} - C_{lm}^{\rho}\right) M\,(2l+1)}{4\pi\, D^2} \left(\frac{R}{D}\right)^l - D \sum_{n=2}^{N} \frac{({}^{(i)}h^n\,\rho)_{lm}}{D^n\, n!} \frac{\prod_{j=1}^{n}(l+4-j)}{(l+3)} \right],$$

for all $l > 0$, where w_l is a filter that removes high-frequency signals resulting from physical processes not accounted for in our model (such as magmatic intrusions and lateral variations in porosity). Since we do not explicitly model the degree 0-potential coefficients, the degree-0 term of ${}^{(i+1)}h\,\rho$ is calculated separately as the average of ${}^{(i)}h\,\rho$. (If the density were constant, this term would be zero.) The function $h\,\rho$ is then expanded on a grid, and the relief $h(\theta,\phi)$ is obtained after dividing by the density contrast $\rho(\theta,\phi)$. To stabilize oscillations between successive iterations, and to speed convergence, the following iterative scheme is used:

$$\begin{aligned} {}^{(i+3)}h &= \left({}^{(i+2)}h + {}^{(i+1)}h\right)/2, && (21) \\ {}^{(i+4)}h &= f\left({}^{(i+3)}h\right), && (22) \end{aligned}$$

where f represents schematically the above described calculation of ${}^{(i+1)}h$. The iteration is initialized using the first-order term of eq. (20).

As an estimate for the grain density of the lunar crust, we make use of Lunar Prospector elemental abundances and an empirical correlation between grain density and composition (see section 1). Given that the most prominent lateral variations in density are associated with broad compositions units, such as the highlands and South Pole-Aitken basin, we use the 5° gridded Lunar Prospector data of ref. [13]. The crust beneath the mare basalts is thought to be broadly anorthositic in composition, and we discard all pixels that contain any such deposits, as well as a few pixels that yield grain densities larger than about 3050 kg m^{-3}. A global grid for the crustal grain density is then obtained by interpolating among the remaining data (Fig. S12). The average grain density of the crust is 2927 kg m^{-3}, and the bulk density is obtained by multiplying each pixel in this map by $(1-\phi)$.

To obtain a unique crustal thickness model, we vary the average thickness of the crust ($R - D$) and the mantle density ρ_m in order to find a solution that fits the seismic constraints at the

Apollo 12 and 14 sites and that has a minimum crustal thickness less than 1 km. The mantle density that is obtained should be considered as being representative only to the minimum radius of the crust-mantle interface, which is less than 80 km below the surface: below this depth, there is no gravitational signature in our model associated with relief along the crust-mantle interface and the mantle density is entirely unconstrained. The degree $\lambda_{1/2}$ at which the filter w_l achieves a value of 0.5 was chosen to be close to 80 in order to minimize high frequency signals that are not accounted for in our model, and that would otherwise be mapped into crustal thickness variations. Furthermore, to avoid noise in the gravity field, the gravity coefficients were truncated above degree 310. All calculations were performed using $N = 7$, and to avoid aliases when computing the spherical harmonic coefficients of $\rho\, h^n$, grids that resolve signals up to spherical harmonic degree 930 were used [49].

Tests show that if lateral variations in crustal density were neglected, long wavelength errors with amplitudes of ± 4 km would arise. In particular, by including lateral variations in density, the thickness of the crust within the South Pole-Aiken basin is about 4 km thicker, and the thickest portion of the farside highlands crust is about 4 km thinner, than would be obtained from a uniform density model. Crustal models constructed using the GRAIL bulk density maps (Fig. 1) give nearly identical average crustal thicknesses as those derived using the grain density map of Fig. S12 and yield lateral variations in thickness that are very similar to those of Fig. 3. Since we do not yet have good constraints on how crustal porosity varies with depth in both the crust and mantle, using the GRAIL bulk densities for the entire crust is not justified at the present time. The neglect of the gravitational signal arising from the dense mare basalts should have only minor consequences on our crustal thickness model. The mare basalts are in general less than 1 km thick [11], and with a density close to that of the mantle, the neglect of the these deposits would only bias the thickness of the crust downward by an amount equal to the thickness of these deposits.

Analyses of the Apollo seismic data initially suggested that the crust was about 60 km thick in the region of the Apollo 12 and 14 landing sites [50], and this value was used as a constraint in several global crustal thickness models following the Clementine mission [26,51,52]. After the Lunar Prospector mission, reanalyses of the Apollo seismic data by two groups showed that the crust was significantly thinner in this region than once thought. Ref. [53] initially suggested a thickness of 45 ± 5 km in the Apollo zone, which was later revised to 38 ± 3 km [24]. An independent analysis by ref. [22] obtained a value of 30 ± 2.5 km, with a later analysis suggesting values of 33 ± 5 and 31 ± 7 km for the Apollo 12 and 14 landing sites [54], respectively. Most subsequent crustal thickness models were not able to fit the revised seismic and minimum crustal thickness constraints, and in retrospect, this was because these studies employed a crustal density between 2800 and 2900 kg m^{-3} that is appropriate for the grain density, but not the bulk density when porosity is considered. Because of this, along with initial skepticism to the revised seismic estimates, most subsequent studies [11,27,55] either employed the 45 km constraint of ref. [53] or ignored the Apollo seismic data altogether. Ref. [54] was successful in reconciling the seismic and crustal thickness modeling, but their study did not consider crustal densities below 2600 kg m^{-3}, and was based on Lunar Prospector-based gravity models that possessed poor resolution over the far side hemisphere.

Several crustal thickness models are summarized in Table S1. The two pre-GRAIL models predict an average crustal thickness of 53 km [11,27] and crustal thicknesses near 45 km at the Apollo 12 and 14 landing sites. Using the grain density map of Fig. S12 with a 12% porosity, and using a 30-km seismic constraint at the Apollo 12 and 14 sites, the average crustal thickness and mantle density are predicted to be 34 km and 3220 kg m^{-3}, respectively. For an assumed porosity of 7%, the average crustal thickness barely changes, but the mantle density increases to 3360 kg m^{-3}. This behavior is easily understood: the largest crustal thickness variations are a result of relief along the crust-mantle interface, and not surface topography, and the amplitude of this relief is controlled by the density contrast between the crust and mantle. A change in crustal density simply trades off to a change in mantle density. Using a seismic constraint of 38 km at the Apollo 12 and 14 sites, the average crustal thickness increases to 43 km, and the mantle density decreases by about 60 kg m^{-3}. For these models, the degree where the filter w_l is 0.5 was reduced to 70 in order to attenuate the amplification of high-frequency signals that occurs when evaluating the gravity field at a deeper crust-mantle interface.

A final crustal thickness model was constructed under the assumption that porosity exists in a layer of constant thickness confined between the surface and depth z. Mathematically, the porosity in this layer is modeled as having a density $-\phi\,\rho_c(\theta,\phi)$, and the gravitational contribution from this void space is added to the other contributions in eq. (18). A gravity signal is generated with a density contrast $-\phi\,\rho_c(\theta,\phi)$ at the surface, and also from an equal an opposite density contrast $\phi\,\rho_c(\theta,\phi)$ with the same relief, but z km below the surface. The density contrast should in fact be $-\phi\,\rho_m$ wherever the crust is thinner than z, but since this only occurs beneath giant impact basins where temperatures could have exceeded the solidus, it is reasonable to use a density contrast with a smaller amplitude in these regions. As with our previous models, the largest variations in crustal thickness are a result of relief along the crust-mantle interface, and not relief along the surface. With the porosity contribution already having been accounted for, the density contrast at the base of the crust is $\rho_m - \rho_c(\theta,\phi)$, which is smaller by $\phi\,\rho_c$ than those used in our previous models. This density contrast is similar to that used in the pre-GRAIL models, and it is not possible to construct a global crustal thickness model that satisfies both the Apollo seismic and minimum crustal thickness constraints, regardless of the values chosen for ϕ and z. If the seismic constraint is ignored, and if the mantle density is set to 3400 kg m^{-3} to maximize the density contrast, an average crustal thickness of ~65 km is obtained, with a thickness close to $\sim$ 57 km at the Apollo 12 and 14 sites.

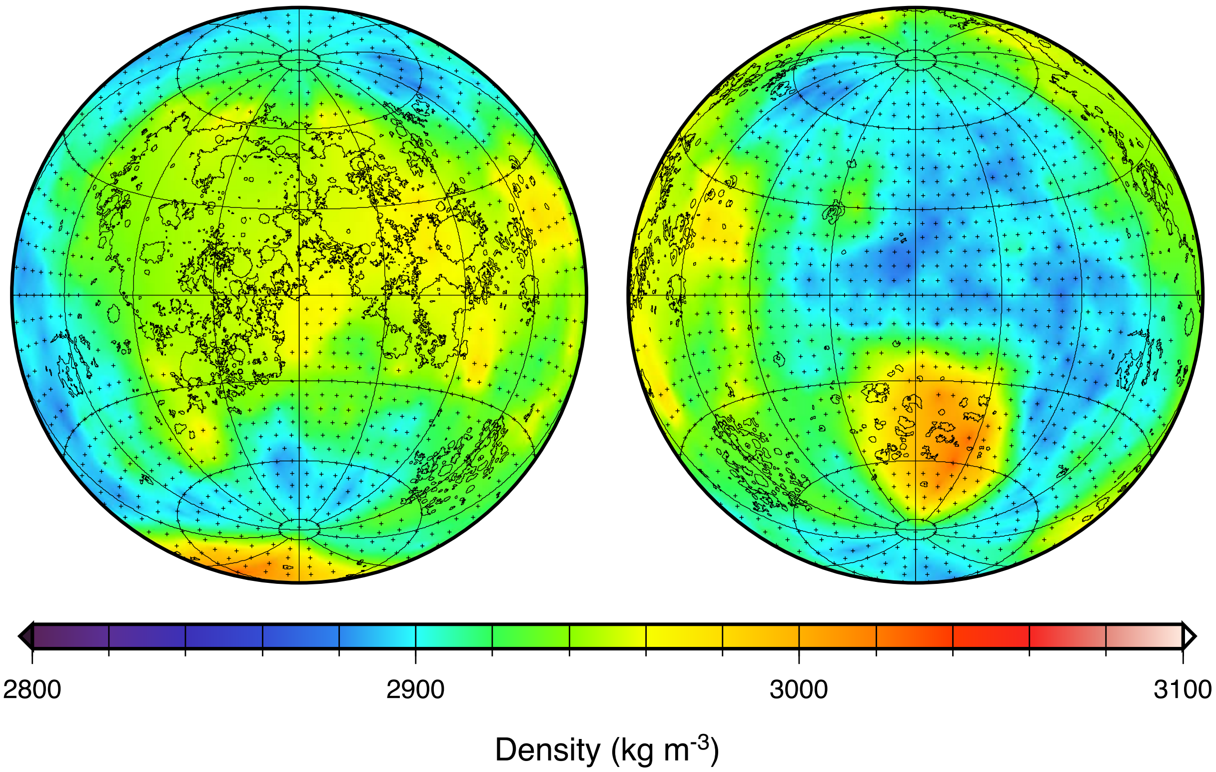

Fig. S12. Grain density of the lunar crust used for constructing a global crustal thickness model. Grain densities exterior to the mare (indicated by the symbol +) were estimated from the 5° Lunar Prospector compositional data along with an empirical correlation between composition and density. After discarding a few pixels with densities greater than about 3050 kg m^{-3}, a global map was determined by interpolating among the remaining data. Image format the same as Fig. S3.

Table S1. Summary of crustal thickness models. Those models that include crustal porosity make use of the crustal grain density map in Fig. S12.

Model	Average thickness, km	Minimum thickness, km	Apollo 12/14 thickness, km	ρ_c or ϕ	ρ_m, kg m^{-3}	$\lambda_{1/2}$
Lunar Prospector gravity, Clementine topography						
Wieczorek et al. (2006)	53.4	0	45	2900 kg m^{-3}	3320	30
Kaguya gravity and topography						
Ishihara et al. (2009)	53	1.2	47.5	2800 kg m^{-3}	3360	50
GRAIL gravity and LRO topography						
Model 1	34	0.6	29.9	12%	3220	80
Model 2	35	0.2	30.8	7%	3360	80
Model 3	43	1.0	38.1	12%	3150	70
Model 4	43	0.5	38.0	7%	3300	70